

Stress Analysis of Contact Deformation in Quasi-Plastic Ceramics

Anthony C. Fischer-Cripps^{*,†} and Brian R. Lawn^{*}

Materials Science and Engineering Laboratory, National Institute of Standards and Technology,
Gaithersburg, Maryland 20899

A stress analysis is made of Hertzian contact deformation in relatively tough ceramics with heterogeneous microstructures, where the response is essentially quasi-plastic rather than ideally elastic–brittle. Contact data for two such heterogeneous ceramics, a micaceous glass-ceramic with modest hardness and a silicon nitride with high hardness, are presented as illustrative cases. Data from a soft steel serve as a comparative baseline. Two distinctive aspects of the deformation response are explored: indentation stress–strain nonlinearity; and size and shape of the damage zone. For the harder ceramics, the stress–strain nonlinearity is less pronounced, and the quasi-plastic zone is more tightly confined beneath the contact, than in traditional ductile metals. As in metals, the deformation process in the ceramic structures is essentially shear driven, but has its origin in microstructurally localized interfacial sliding faults rather than in dislocation slip. Finite element modeling (FEM) is used to compute the shear stress distributions beneath the spherical indenters for selected experimental loading conditions. The underlying basis of the FEM calculations is an elastic–plastic constitutive relation based on a critical shear condition for yield, but incorporating a strain-hardening characteristic to allow for local elastic constraints on the sliding shear faults. The FEM calculations are able to simulate the main features of the stress–strain curves and the evolving deformation zone geometries. In addition, the calculated tensile stress distributions are able to account, at least in part, for the suppression of conventional brittle fracture tendencies in tougher ceramics.

I. Introduction

CERTAIN heterogeneous ceramics which respond in an ordinarily brittle fashion in tension fields undergo a distinctive transition to a quasi-plastic response in confined compression fields.¹ Such transitions toward “ductility” in otherwise brittle materials have a well-documented precedent in rock mechanics, where confining compression states are the norm rather than the exception.^{2–5} Macroscopically, quasi-plasticity in ceramics resembles conventional plasticity in metals, in that it is shear driven. Microscopically, the underlying source of deformation is dissipative slip at microstructurally discrete “shear faults,” e.g., weak particle/matrix interfaces or twin planes, augmented by internal residual stresses.^{6–13} These are the same microstructural ingredients as those responsible for *R*-curves from crack-interface bridging,^{14–16} so there is a basic connection between quasi-plasticity and (long-crack) toughness. The quasi-plasticity in these materials is manifested as a “yield” point in the intrinsic stress–strain curve, identifiable with first slip at the

discrete fault interfaces, but with significant strain-hardening, from matrix constraint on this slip.^{12,17} It is implicit that such quasi-plasticity can be controlled by judiciously tailoring the ceramic microstructure (“microstructural design”).^{1,17}

The nature of quasi-plasticity in heterogeneous ceramics is demonstrated most compellingly in the deformation fields of contacts with spherical indenters.^{1,7,9,10,13,18} Instead of the cone cracks *outside* the contact that typify ideally brittle solids,¹⁹ a damage zone initiates and expands *beneath* the contact, strongly reminiscent of the plastic zone in metals.²⁰ The subsurface stress field where the damage accumulates contains a large component of shear, but no tension. The degree of yield can be quantified on an indentation stress–strain curve,^{8,10} as a deviation from the Hertzian linear elastic response. The characterization of quasi-plasticity in contact fields is therefore of prime importance to the physical understanding of basic deformation modes in tough ceramics. It also offers critical insights into a broad range of practical contact-related problems, such as the lifetime of ceramic bearings, the mechanisms of machining and wear, and the susceptibility to impact and fatigue damage.^{9,11–13,21–24}

The mechanics of quasi-plastic indentation in heterogeneous ceramics have not been addressed in the literature. On the other hand, indentation plasticity models for metals have been available for over half a century. Even there the models represent ideal cases, depending on the ratio of yield stress to elastic modulus, Y/E . For soft metals (low Y/E), plasticity dominates and the displaced material piles up around the indenter. The indentation stress–strain curve flattens out beyond the yield point, rising to a limiting contact pressure (indentation “hardness”) $H \approx 3Y$ at “full plasticity.”^{20,25} Traditional slip-line field models for rigid-plastic solids describe the deformation geometry sufficiently well in this limit.^{20,25,26} For hard metals (intermediate Y/E), pileup is largely suppressed and the plastic material displaces radially outward from the indentation origin, engulfing the contact area at full plasticity. The indentation stress–strain curve is somewhat steeper, and the “constraint factor” H/Y is no longer material-independent.²⁷ In this case it becomes necessary to take into account the constraint of the confining elastic surrounds on the radially expanding plastic zone. Centrosymmetric “expanding cavity” models for elastic–plastic solids provide adequate solutions for this class of material.^{20,25,26,28} In heterogeneous ceramics (moderately high Y/E), pileup is again largely absent but the quasi-plastic zone is markedly more constricted beneath the contact.¹ Deviations from Hertzian linear elasticity in the indentation stress–strain response are much less pronounced, indicating an even more dominant elastic component in the contact deformation. The traditional indentation plasticity models contain no clear provision for such distinctive features of the damage response in hard ceramics.

In view of the complexity of the contact quasi-plasticity processes envisaged in the class of ceramic materials of interest here, resort to numerical protocols for analysis seems unavoidable.²⁹ In this paper we carry out such a numerical analysis, using finite element modeling (FEM).^{30–32} For illustrative case studies, we choose two model ceramics previously shown to

M. Thouless—contributing editor

Manuscript No. 192098. Received January 9, 1996; approved March 26, 1996.

Supported by the U.S. Air Force Office of Scientific Research.

^{*}Member, American Ceramic Society.

[†]Guest scientist from the Department of Materials Science and Engineering, Lehigh University, Bethlehem, Pennsylvania 18015. Now in the Department of Applied Physics, University of Technology at Sydney, Sydney, NSW 2007, Australia.

exhibit quasi-plasticity: a moderately soft micaceous glass-ceramic;^{8,9} and a considerably harder but nevertheless deformable silicon nitride.¹³ A soft steel is included as a comparative baseline. We focus on the two distinctive features of the deformation mechanics for heterogeneous ceramics referred to above: the more constricted deformation zone geometry; and the steepened indentation stress-strain curve. In accounting for these features, the FEM methodology allows full determination of the stress redistribution in and around the yield zone, and enables extraction of the constitutive stress-strain function for a given ceramic material.

II. Contact Deformation in Heterogeneous Ceramics

(1) Materials

In this section we summarize pertinent experimental contact damage results from previous studies on two model heterogeneous ceramic materials, both with enhanced long-crack toughness and with attendant capacity to produce quasi-plastic Hertzian indentations:

(i) *Micaceous glass-ceramic.*^{8,9} A glass-ceramic of modest hardness, with ≈ 55 vol% interlocking fluorophlogopite mica flakes 10 μm long and 1 to 2 μm thick in a matrix of ≈ 45 vol% borosilicate glass (Macor, Corning Inc., Corning, NY).^{33,34} The mica flakes with their weak basal cleavage and matrix interphase boundaries facilitate easy microfailure at the microstructural level, rendering the material machinable and highly susceptible to irreversible contact deformation.

(ii) *Silicon nitride.*¹³ A much harder ceramic, yttria-doped (4 vol%) hot-isostatically-pressed and heat-treated to produce coarsened, elongated β -phase grains with width ≈ 2.0 μm and aspect ratio 4 to 5.¹³ The grains are susceptible to shear failure by twinning or crystallographic slip, and the intergrain phase is weak and glassy and susceptible to shear deformation and attendant microcracking.

In addition, we present contact test data for a soft steel with negligible strain-hardening,²⁰ to establish an ideal elastic-plastic baseline for comparison with the ceramic materials. We also present data for tungsten carbide specimens cut from the spherical indenters (Section II(2)), to calibrate the indenter material; this latter is necessary because the indenter itself is susceptible to plastic deformation, especially in tests on the harder ceramics.

Essential properties are included in Table I. Young's modulus E and Poisson's ratio ν are from independent measurements, indentation hardness H is evaluated as load/projected contact area²⁰ from Vickers indentations, yield stress Y is determined from observations of first deformation below the contact in sequential load experiments,^{20,35} and strain-hardening coefficient α is an adjustable parameter (Section III).

(2) Indentation Stress-Strain Curves

The Hertzian test can be used to obtain indentation stress-strain curves for a given material.^{7,8} Tungsten carbide spheres (J&L Industrial Supply, Livonia, MI) are used to produce contacts in polished specimen surfaces, at prescribed loads P and sphere radii r . Contact radii a are measured from impressions left in thin metal coatings on the specimen surfaces. These measurements enable plots of mean indentation pressure

$p_0 = P/\pi a^2$ versus indentation strain a/r . The uncertainty in measurement of a is $\approx 5\%$, corresponding to $\approx 5\%$ in a/r and $\approx 10\%$ in p_0 .

Experimental indentation stress-strain results from contact tests on the test materials listed in Table I, using sphere sizes in the range $r = 1.98$ to 12.7 mm, are reproduced as data points in Figs. 1 to 4. The data fall on universal curves, independent of sphere size, in accordance with the principle of geometrical similarity for contacts on bodies with spatially invariant properties.^{6,20,36} In considering these results it is useful to recall that homogeneous brittle solids like glass closely follow an ideally linear elastic response (Hertzian elasticity, see Section III(2)).⁸ Varying degrees of departure from such a linear response are observed in Figs. 1 to 4. In the steel, Fig. 1, the initial elastic region is extremely limited, with a dominant yield bendover. In the glass-ceramic, Fig. 2, the elastic region extends over a greater range of stress and strain, and the plasticity characteristic, while not as strong as in the steel, is nevertheless still pronounced. In the silicon nitride, Fig. 3, the elastic region extends still further, and the nonlinear deviation at higher stresses and strains is now relatively mild. This tendency to a diminishing plasticity component in the materials sequence of Figs. 1 through 3 correlates with increasing value of Y/E in Table I.

Finally, in the tungsten carbide, Fig. 4, the data again show an extensive initial elastic region, but still with a perceptible deviation at higher stresses and strains. Accordingly, we may expect that tungsten carbide indenters themselves suffer plastic flow in tests on harder ceramics, specifically on the silicon nitride in Fig. 3 and on the like tungsten carbide in Fig. 4.

(3) Observations of Contact Damage Zones

Revealing views of damage accumulation from indentation tests are most readily obtained using a "bonded-interface" technique.^{7,8,37} Two polished half-blocks cut from a given specimen

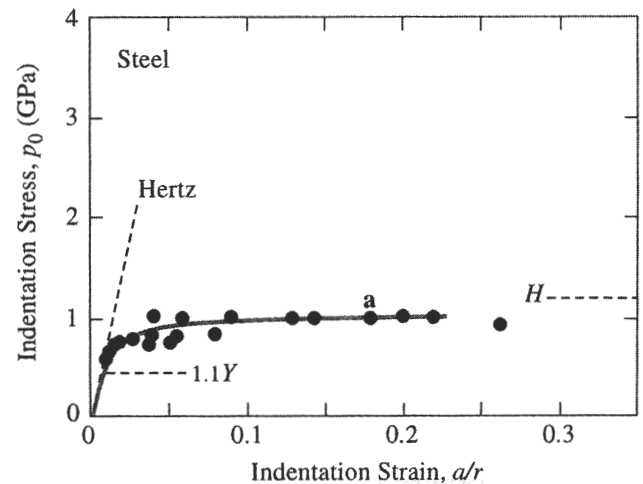


Fig. 1. Hertzian indentation stress-strain curve for tungsten carbide spheres on soft steel. Data points are experiment measurements (sphere radii $r = 1.98$ to 12.7 mm, not distinguished). Solid curve is FEM fit ($\alpha = 0$). Dashed lines indicate Hertzian elastic response, initial yield pressure, and Vickers indentation hardness. Point a corresponds to contact conditions in micrograph in Fig. 5.

Table I. Elastic and Yield Parameters for Materials Used in Finite Element Modeling[†]

Material	Young's modulus E (GPa)	Poisson's ratio ν	Hardness H (GPa)	Yield stress Y (GPa)	Work-hardening coeff α
Glass-ceramic [‡]	63	0.26	2.8	0.77	0.10
Silicon nitride [§]	320	0.27	15	7.3	0.50
Steel [¶]	210	0.30	1.1	0.39	0
Tungsten carbide ^{††}	614	0.22	19	6.0	0.10

[†] E and ν from independent supplier specifications (see cited references); H from Vickers impressions (load/projected area); Y from critical contact pressure at first yield; and α from best fit to indentation stress-strain data. [‡]References 8 and 9. [§]Reference 13. [¶]Reference 32. ^{††}Indenter material. References 8 and 9.

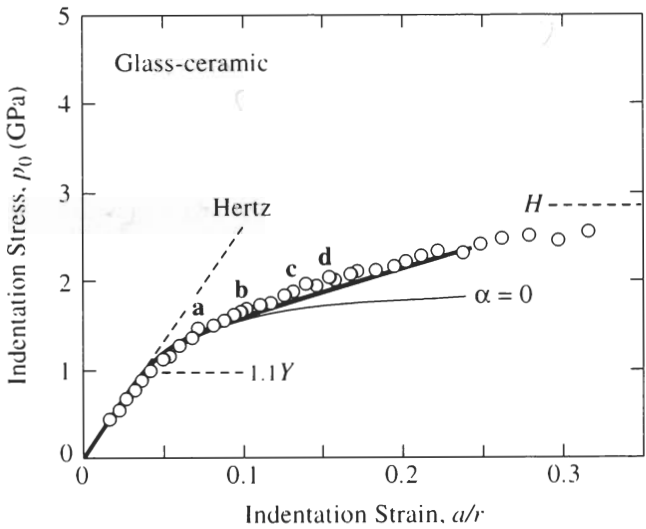


Fig. 2. Hertzian indentation stress-strain curves for micaceous glass-ceramic. Data points are experiment measurements (sphere radii $r = 1.98$ to 12.7 mm, not distinguished). Solid curves are FEM fits ($\alpha = 0$ and $\alpha = 0.10$). Dashed lines indicate Hertzian elastic response, initial yield pressure, and Vickers indentation hardness. Points a, b, c, d correspond to contact conditions in micrographs in Fig. 6. Data reproduced from Refs. 1 and 8.

are glued together at their sides with adhesive, and top-surface indentations then made along the interface trace with a tungsten carbide sphere of radius $r = 1.98$ or 3.18 mm. The indented half-blocks are separated by immersion in solvent, and gold-coated for viewing in the optical microscope using Nomarski contrast illumination.

Half-surface and subsurface views obtained in this way for the reference steel are shown in Fig. 5, at an indentation strain $a/r = 0.18$, i.e., well into the plasticity region (cf. Fig. 1).³² A well-defined impression is evident in the top view. There is little indication in the Nomarski illumination of any significant pileup around this impression. In the side view the plastic zone extends downward and outward well beyond the contact on a

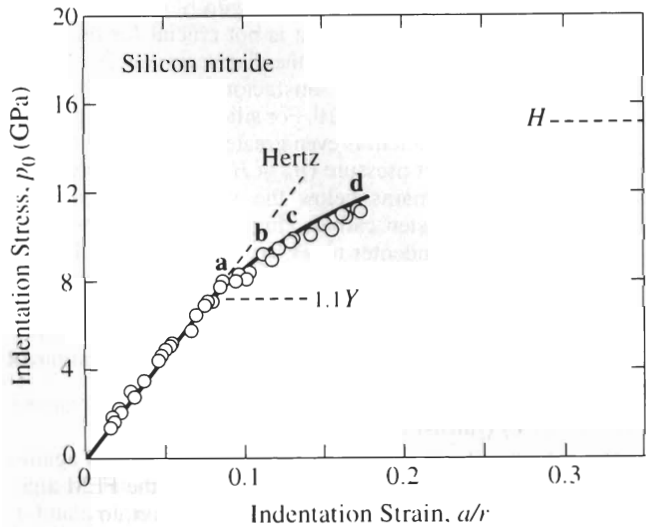


Fig. 3. Hertzian indentation stress-strain curves for heterogeneous silicon nitride. Data points are experiment measurements (sphere radii $r = 1.98$ to 12.7 mm, not distinguished). Solid curve is FEM fit ($\alpha = 0.50$). Dashed lines indicate Hertzian elastic response, initial yield pressure, and Vickers indentation hardness. Points a, b, c, d correspond to contact conditions in micrographs in Fig. 7. Data courtesy of N. P. Padture, H. H. K. Xu, and S.-K. Lee.

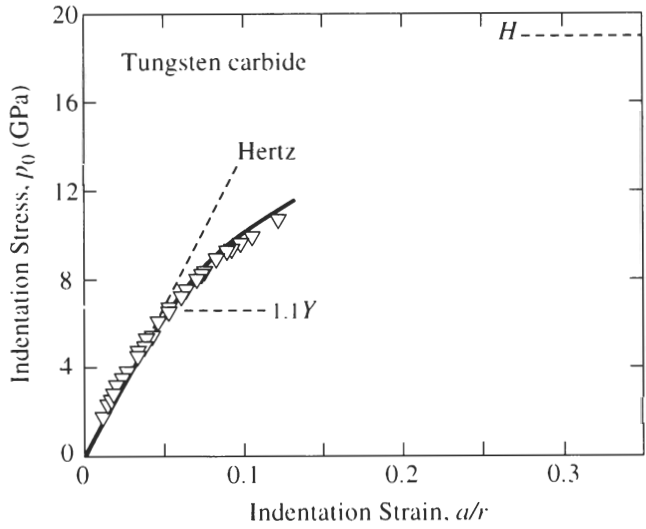


Fig. 4. Hertzian indentation stress-strain curve for tungsten carbide. Data points are experiment measurements (sphere radii $r = 1.98$ to 12.7 mm, not distinguished). Solid curve is FEM fit ($\alpha = 0.10$). Dashed lines indicate Hertzian elastic response, initial yield pressure, and Vickers indentation hardness. Data courtesy of M. Stevens Kalceff, F. Guiberteau, and N. P. Padture.

near-hemispherical front, albeit with some “pinching in” just below the top free surface.

Comparative views for the glass-ceramic are shown in Fig. 6 and for the silicon nitride in Fig. 7, for load sequences extending well into the plasticity region (cf. Figs. 2 and 3). Surface impressions are clearly apparent in the top view in both these materials, although they appear more clearly developed in the softer glass-ceramic. Again, there is no evidence of pileup. Indications of incipient ring crack formation are apparent around the contact in the silicon nitride. The side views reveal how the deformation zone initiates below the contact at low

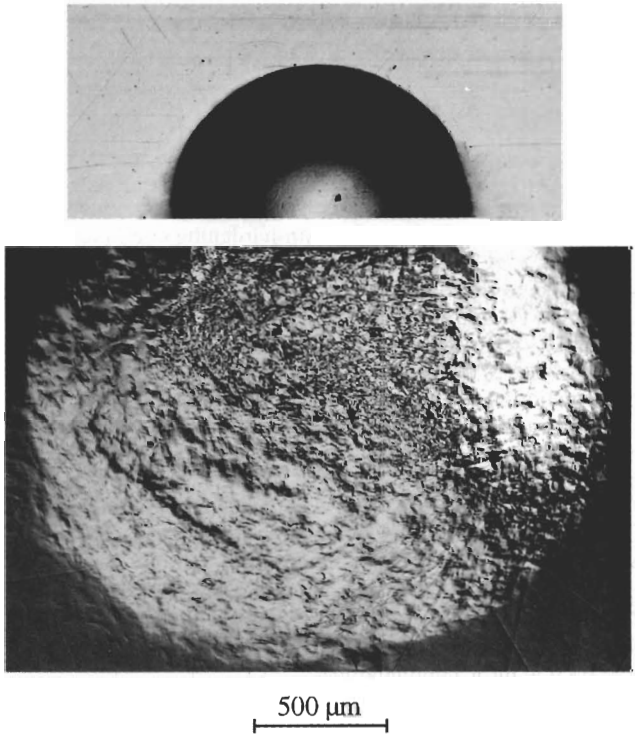


Fig. 5. Half-surface and side view of indentation in soft steel with tungsten carbide sphere, radius $r = 3.18$ mm, load $P = 1000$ N. Bonded-interface specimen, Nomarski interference.

load, as anticipated from the subsurface location of maximum shear stress within the Hertzian stress field,^{6,8,20,35,36} and progressively expands as the load increases. In neither ceramic does the developed subsurface deformation zone extend beyond the contact area a at the top surface, although in the glass-ceramic the zone is less constricted below the surface. Note in the silicon nitride there is no evidence in the side views for development of the surface ring cracks into deep cone cracks.

Load sequences such as those in Figs. 6 and 7 also enable determination of at least an upper bound to the critical stress conditions for the onset of quasi-plastic deformation. This method is used to determine the yield stress (Section III(2)) for each material in the present study.

Post-test examination of the tungsten carbide spheres confirms substantial flattening from contacts on the silicon nitride and tungsten carbide specimens, but not on the glass-ceramic or steel.

III. Finite Element Analysis

(1) FEM Code

Finite element computations in this study of elastic-plastic contacts are carried out using a commercial package (Strand, G&D Computing, Sydney, Australia).³² The configuration modeled is that of a sphere of specified radius in axisymmetric frictionless contact with the flat surface of a half-space, 4 mm \times 4 mm \times 4 mm. The mesh in the half-space consists of 1736 nodes and 1538 axisymmetric quadrilateral plate elements, with a greater concentration of cells in the vicinity of the contact, Fig. 8. Loading proceeds from initial contact in a stepwise manner, with a maximum 50 iterations per increment to allow for relaxation to equilibrium at each step. A special feature of the present algorithm is that, by the use of "gap elements,"³² the expanding contact is adjusted automatically without *a priori* knowledge of the radius of the contact circle. Tolerance levels for the iterative computations are set at 0.1% for the node forces and 0.5% for the displacements.

Plastic deformation in the test material, and also in the indenting sphere, is governed in our calculations by a critical shear stress criterion with linear strain-hardening. This criterion is accommodated within the finite element code by imposing a generic uniaxial compression stress-strain response $\sigma(\epsilon)$ for each material (including indenter):

$$\sigma = E\epsilon \quad (\sigma < Y) \quad (1a)$$

$$\sigma = Y + \alpha(\epsilon E - Y) \quad (\sigma > Y) \quad (1b)$$

with E Young's modulus, Y the uniaxial stress for the onset of yield, and α a dimensionless strain-hardening coefficient in the range $0 \leq \alpha \leq 1$ ($\alpha = 0$, fully plastic; $\alpha = 1$, fully elastic). We will return to the issue of a linear strain-hardening component in Section IV, and simply note at this point that physical justification for such a component is forthcoming from micromechanical analyses of the underlying discrete slip events.¹⁷ Nonlinear deformation is accommodated in the algorithm by considering all cells in both specimen and indenter to deform elastically, but redefining a local modulus σ/ϵ from Eq. (1b) ("secant method").³²

Computational uncertainties associated with limits on the operating tolerances and grid sizes amount typically to $\approx 3\%$ in contact radius, corresponding to $\approx 6\%$ in stress and $\approx 3\%$ in strain, with a tendency to greater values in the plastic region as the strains increase. Slower convergence in the high-strain plastic region limits the upper range of indentation loads that can be accessed in these computations.

(2) Computation of Indentation Stress-Strain Curves

In this section we generate indentation stress-strain curves for the materials in Figs. 1 to 4 from the FEM code. First we set the following bounding states, represented as the dashed lines in the figures:²⁰

(i) *Hertzian elasticity*. The response at low stresses is according to the classical linear Hertzian relation^{36,38}

$$p_0 = (3E/4\pi k)a/r \quad (2)$$

where $k = (9/16)[(1 - \nu^2) + (1 - \nu'^2)E/E']$ is a dimensionless coefficient, with the prime notation denoting the indenter material. Because the elastic constants are generally specifiable *a priori* for a given indenter/specimen material system, the stress-strain relation in Eq. (1) is predetermined. Note that the value of k , hence the slope of the stress-strain curve in the initial linear region, is dependent on the indenter material.

(ii) *Yield point*. According to the critical shear criterion, the onset of conventional plasticity is predicted to occur when the maximum shear stress $\approx 0.47p_0$, located at a depth $\approx 0.5a$ below the contact axis, reaches one half the uniaxial yield stress Y , corresponding to a point of deviation $p_0 \approx 1.1Y$ on the stress-strain curve.^{20,35} The yield stress Y is therefore calculable from experimental determination of the critical contact pressure for initiation of subsurface irreversible deformation (Section II(3)).

(iii) *Full plasticity*. At large contact stresses, the deformation tends more toward a response for rigid-plastic materials, saturating at a level $p_0 = cY$, where c is a constraint factor. This saturation level is approximated by the hardness values H from Vickers indentations (Section II(1)).²⁰ For very soft metals the constraint factor is $c \approx 3$, but as indicated earlier (Section I) may be expected to vary significantly in ceramics as the geometrical aspects of the contact change.

The only quantity in Table I that is not predetermined in the FEM computations is the strain-hardening coefficient α , which we adjust to best-fit the experimental data in the nonlinear region of the indentation stress-strain curve for each material. This is done first for the tungsten carbide material in Fig. 4, because tungsten carbide spheres are common to all tests. The fit is obtained by incrementing α in steps of 0.05 and selecting the value with least variance. A more accurate determination than this is considered unwarranted, in view of the aforementioned uncertainties inherent in both the data and the algorithm. Each indentation stress-strain curve is generated by determining the equilibrium contact radius at each load step, evaluating corresponding indentation stresses p_0 and indentation strains a/r , and smoothing the discrete results.

The FEM functions thus generated are plotted as the solid curves in Figs. 1 to 4. These curves fit the data points within the limits of experimental and computational scatter. For the soft steel, Fig. 1, we obtain an adequate fit with $\alpha = 0$, confirming that a strain-hardening component is not crucial for this near-ideal elastic-plastic material. For the glass-ceramic, Fig. 2, it is no longer possible to obtain a satisfactory fit with $\alpha = 0$; the best fit is obtained with $\alpha = 0.10$. For silicon nitride, Fig. 3, the strain-hardening coefficient is even greater, $\alpha = 0.50$. Note that the upper level contact pressure ($p_0 \approx H$) in both the steel and the glass-ceramic remains below the yield contact pressure ($p_0 \approx 1.1Y$) for tungsten carbide (Fig. 4), consistent with the observation that the indenter never exceeds the elastic limit in contacts on these two materials. In the silicon nitride and tungsten carbide, however, the contact stresses extend well beyond the yield point of the indenting material, so part of the nonlinearity in these materials is inevitably due to deformation of the sphere.

(3) Shape of Quasi-Plastic Zone

Once the "calibrations" of the parameters in Eq. (1) against the indentation stress-strain data are complete, the FEM algorithm enables evaluation of the principal stresses σ_1 , σ_2 , and σ_3 ($\sigma_1 \geq \sigma_2 \geq \sigma_3$ everywhere except in the free-surface region, where $\sigma_2 < \sigma_3 = 0$ ³⁹) in the contact fields. Our primary interest lies in the maximum shear stress τ , defined in the broader subsurface region by $\tau_{31} = \frac{1}{2}(\sigma_3 - \sigma_1)$ and in the near-free-surface region by $\tau_{12} = \frac{1}{2}(\sigma_1 - \sigma_2)$. We are expressly interested in the contour $\tau = Y/2$ defining the boundary of the yield zone. The maximum principal stress in the tensile regions, $\sigma_1 > 0$, is

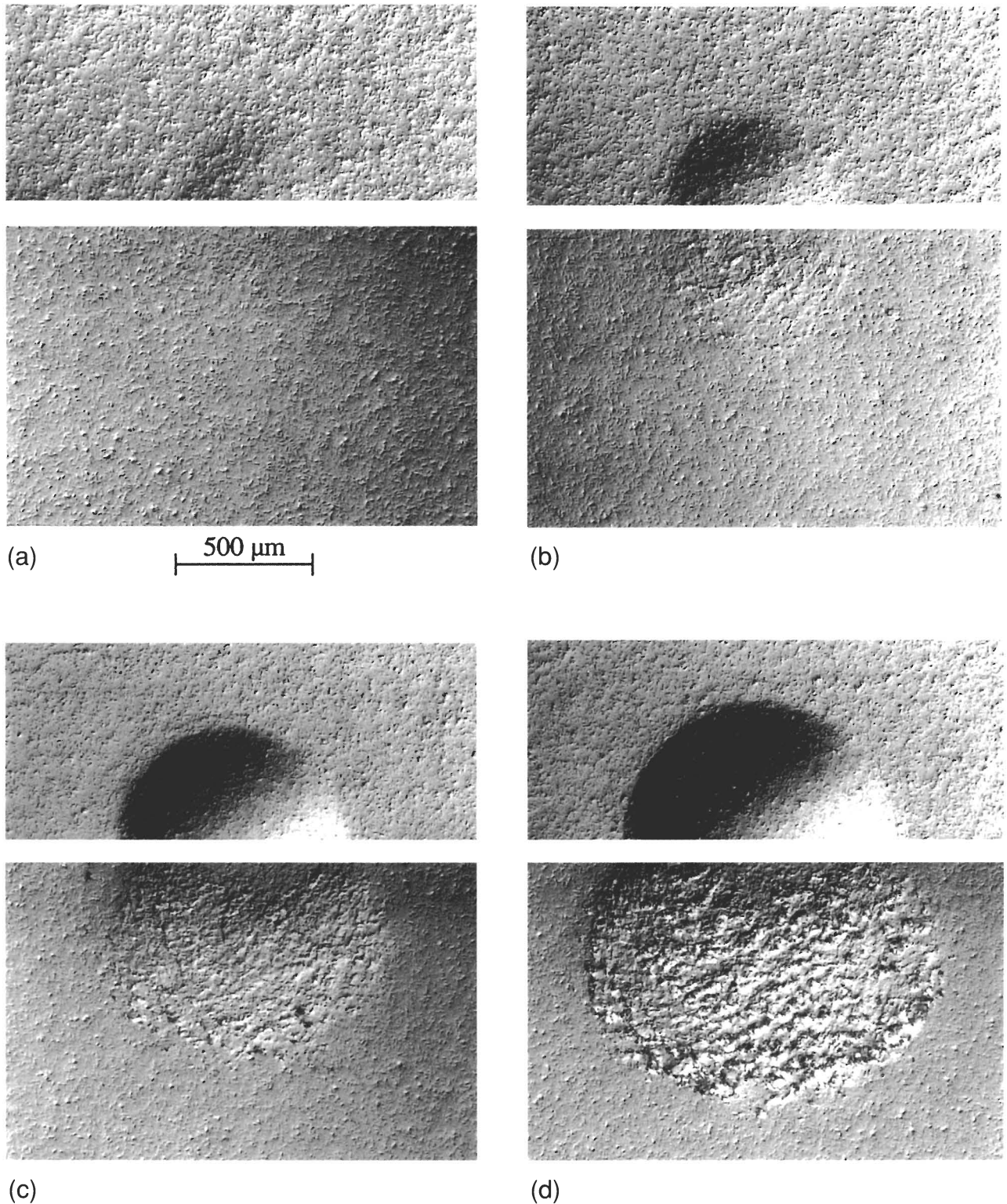
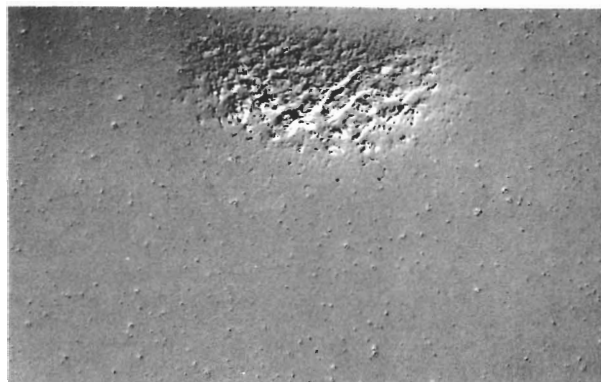
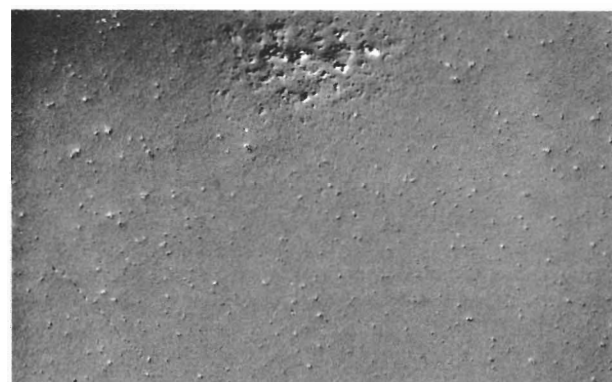
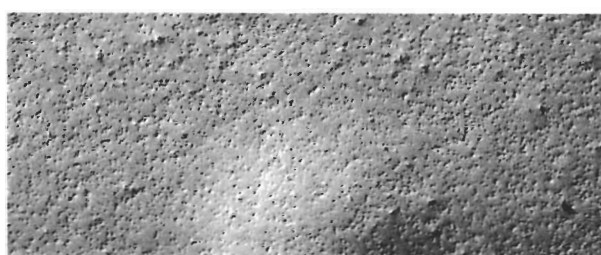
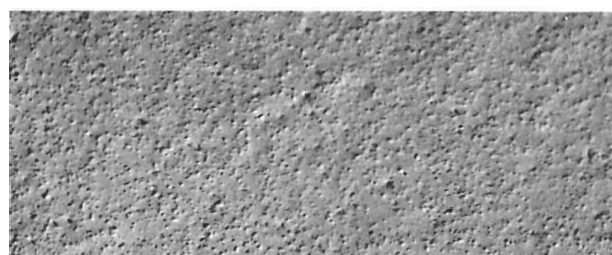


Fig. 6. Half-surface and side view of indentation in micaceous glass-ceramic with tungsten carbide sphere, radius $r = 1.98$ mm, loads (a) $P = 250$ N, (b) 500 N, (c) 1000 N, (d) 1500 N. Bonded-interface specimen, Nomarski interference. Micrographs reproduced from Ref. 8. Reprinted with the permission of the Materials Research Society.

of some interest also, in relation to any attendant fracture patterns. In plotting stress contours an internode interpolation procedure is used to smooth out grid discreteness.³²

Contours of yield zone boundaries are accordingly plotted in Figs. 9 to 11 for each of the test materials, at the same loads and sphere radii as used to obtain the micrographs in Figs. 5 to 7. For the steel, we observe that the calculated contour in Fig. 9 reproduces all the major geometrical features of the fully developed plastic zone observed in the section view of Fig. 5. The

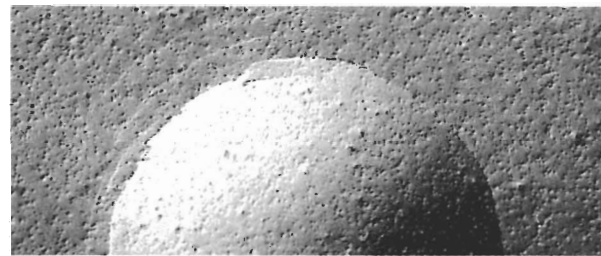
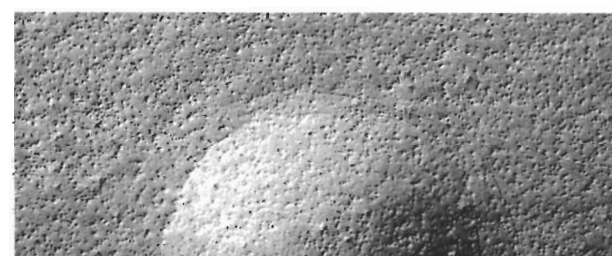
zone boundary extends well beyond the contact circle on an approximately hemispherical front centered about the contact origin. There is a distinctive pinching in just below the specimen outer free surface, where τ switches from τ_{31} to τ_{12} .²⁹ The FEM computation predicts $\approx 15\%$ smaller zone size than that observed (cf. depth ≈ 1.3 mm in Fig. 9 with ≈ 1.5 mm in Fig. 5), but this level of discrepancy is hardly beyond the bounds of combined experimental and computational uncertainties cited earlier.



(a)

(b)

500 μm



(c)

(d)

Fig. 7. Half-surface and side view of indentation in heterogeneous silicon nitride with tungsten carbide sphere, radius $r = 1.98$ mm, loads (a) $P = 1000$ N, (b) 1500 N, (c) 2000 N, (d) 3000 N. Bonded-interface specimen, Nomarski interference. Micrographs courtesy of N. P. Padture.

For the glass-ceramic and silicon nitride, Figs. 10 and 11, respectively, significant departures from an essentially hemispherical quasi-plastic zone geometry are apparent. Again, the FEM contours reproduce all the major geometrical features of the evolving damage zones in the corresponding micrographs in Figs. 6 and 7. The predicted tendency for the damage to initiate below the specimen surface at a critical contact pressure, and subsequently to expand into a fully plastic zone at

higher pressures, is apparent in the computed contours, most noticeably in the harder silicon nitride. The constriction of the damage zone to the immediate subsurface contact region is manifest, again most strongly in the silicon nitride, reflecting an enhanced elastic constraint. Note that the contours for the glass-ceramic do nevertheless retain some of the remnant features of the zone geometry in the steel, namely the characteristic subsurface bulge with near-surface pinching, consistent with an

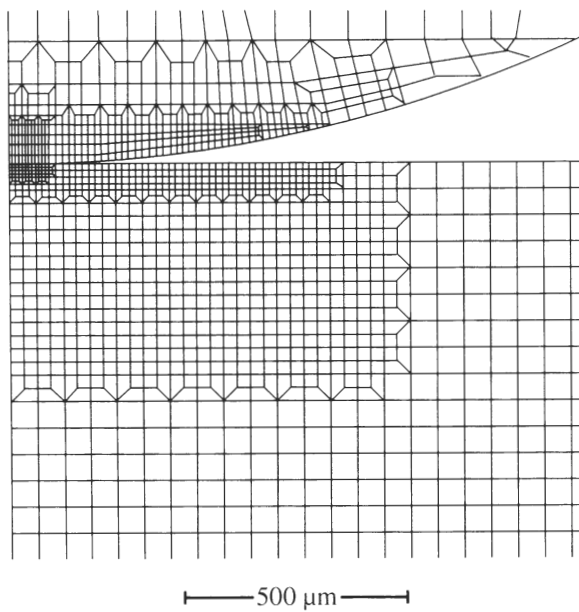


Fig. 8. Finite element model (FEM) mesh, showing portion of half-section. Grid shown for sphere radius $r = 3.18$ mm. Note greater concentration of elements in contact zone.

intermediate value of Y/E in Table I. Discrepancies between calculated and observed zone sizes (depths) are less than 10% at any load in either of the ceramics.

A closer look at the FEM-generated stress fields provides some insights into the deformation processes in ceramics, and allows us to explore potential changes in these processes with variation in elastic-plastic constants. Consider the extreme case of silicon nitride. Recall that the limited quasi-plasticity in the specific silicon nitride used in the present study is attributable to a somewhat coarsened microstructure (Section II(1)¹³), with strain-hardening coefficient $\alpha = 0.50$ (Section III(2)). Figure 12 plots contours of shear stress τ (upper diagram) and normal stress σ_1 (lower diagram) for this silicon nitride, at the highest

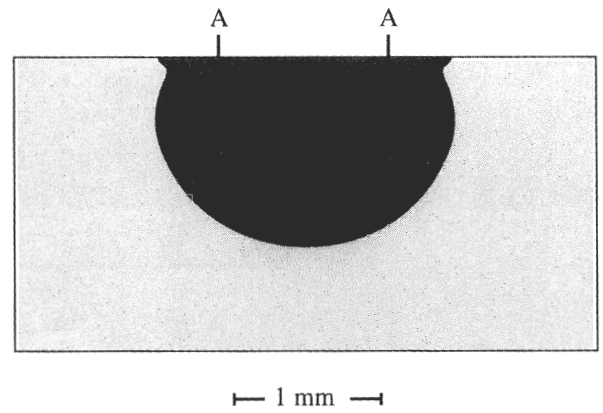


Fig. 9. FEM-generated yield zone boundary for indentation in soft steel with tungsten carbide sphere, radius $r = 3.18$ mm, load $P = 1000$ N. Contact diameter AA. Cf. micrograph in Fig. 5.

contact load (3000 N) represented in Figs. 7 and 11. The shading indicates yield ($\tau > Y/2$) and tension ($\sigma_1 > 0$) zones, respectively. Note that the shear stresses continue to build up within the highly confined yield zone, because of the strain-hardening. Now compare these contours with those plotted in Fig. 13 for a hypothetical homogeneous silicon nitride with the same elastic constants but with $\alpha = 1$ in Eq. (1), i.e., for an ideal Hertzian elastic solid. The buildup of subsurface shear stresses is noticeably stronger in the latter case, consistent with an ideally linear stress-strain response without quasi-plasticity. More profound differences in Figs. 12 and 13 are evident in the σ_1 contours, especially in the expanded subsurface compressive zone for the heterogeneous test silicon nitride material in Fig. 12. The corresponding shallowing of the outer tensile zone, attributable to stress relaxation around the subsurface yield zone, may be part of the reason why the surface ring cracks in Fig. 7 are unable to propagate into full cone cracks.

Analysis of the FEM surface displacements outside the indentations reveals no significant pileup outside the indentations in any of the test materials, including the steel, consistent with the experimental observations in Section II(3).

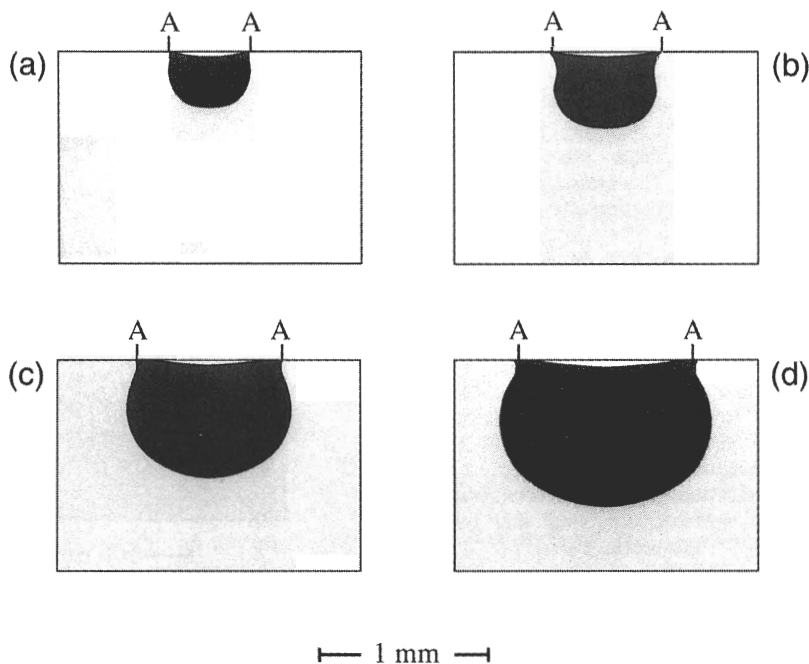


Fig. 10. FEM-generated yield zone boundary for indentation micaceous glass-ceramic with tungsten carbide sphere, radius $r = 1.98$ mm, loads (a) $P = 250$ N, (b) 500 N, (c) 1000 N, (d) 1500 N. Contact diameter AA. Cf. micrographs in Fig. 6.

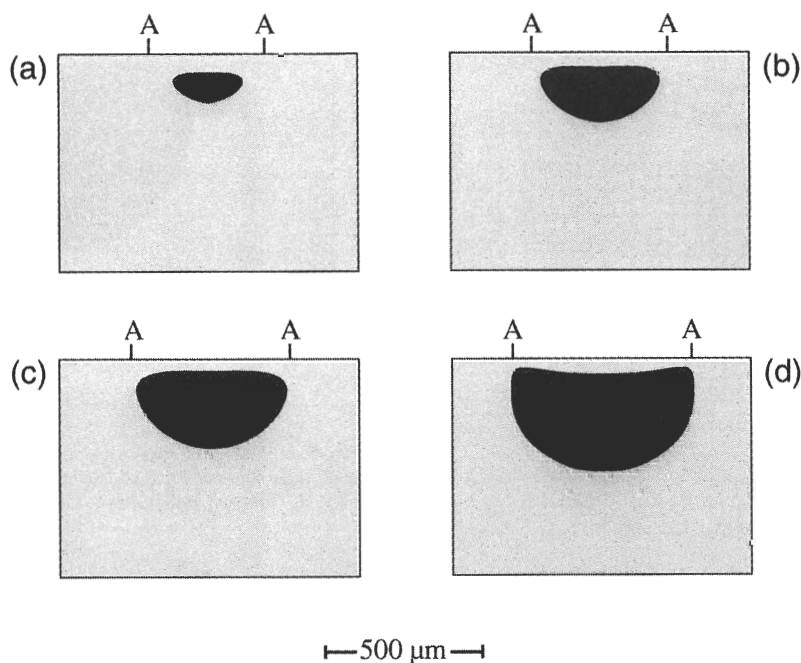


Fig. 11. FEM-generated yield zone boundary for indentation in heterogeneous silicon nitride with tungsten carbide sphere, radius $r = 1.98$ mm, loads (a) $P = 1000$ N, (b) 1500 N, (c) 2000 N, (d) 3000 N. Contact diameter AA. Cf. micrographs in Fig. 7.

IV. Discussion

We have presented a stress analysis of quasi-plastic deformation in tough, heterogeneous ceramics. Specifically, we have accounted for the macroscopic features of deformation beneath Hertzian contacts using FEM. The analysis definitively identifies the shear component of the stress field as the underlying driving force for the deformation. This is the same shear component that drives traditional plasticity at contacts in metals. However, the corresponding deformation in ceramics occurs at significantly higher stresses (higher Y/E), and in a much more constricted zone below the contact. Moreover, the underlying nature of the deformation differs fundamentally from that in metals. Hence the designation “quasi-plasticity,” or “quasi-ductility”.¹ We reemphasize the unique capacity of the Hertzian test as a means of characterizing the transition to shear-driven subsurface quasi-plasticity from classical tension-driven cone fracture with increasing microstructural heterogeneity. In conventional stress-strain tests, premature brittle failure generally precludes the detection of any quasi-plasticity at all, except in those ceramics where the nonlinearity is extreme (e.g., phase-transforming zirconias^{40,41} and two-phase materials with uncommonly high internal stresses⁴²). The Hertzian test also provides critical information on the entire stress-strain function $p_0(a/r)$ (Figs. 1 to 4), in the evolution of deformation from initial elastic to fully plastic; the Vickers test, by comparison, provides information only on the fully plastic state at $p_0 \approx H$.

As intimated above, the intrinsic microstructural units of slip that underlie quasi-plasticity in heterogeneous ceramics differ fundamentally from dislocation slip in metals.¹ These units are identifiable as discrete “shear faults” in the microstructure—weak internal surfaces or interfaces subject to frictional sliding. For the specific glass-ceramic⁸ and silicon nitride¹³ studied here, the active fault configuration consists mainly of a dense network of weak matrix/second-phase interfaces. More generally, the faults can be either intrinsic (e.g., weak intergrain or interphase boundaries,^{8,10,11,13,43} intragrain twins)^{6,7,13,44} or extrinsic (preexisting cracks or voids in rocks or porous ceramics^{2,3,45–49}). In all such cases, the slip at each fault is locally constrained by the surrounding elastic matrix, so the individual shear displacements are limited by the microstructural scale of the faults. Generic shear fault models^{12,17,50} provide a micro-mechanical basis for expressing this slip in terms of the macroscopic parameters Y and α in Eq. (1): yield stress Y is

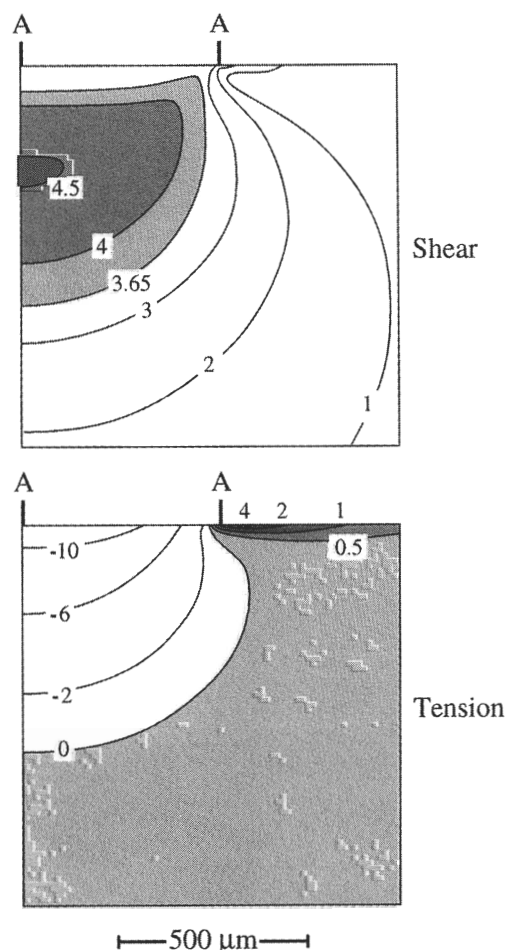


Fig. 12. FEM-generated stress contours in heterogeneous silicon nitride ($\alpha = 0.50$) indented with tungsten carbide sphere, radius $r = 1.98$ mm, load $P = 3000$ N. Stresses in units of GPa. Upper diagram plots maximum principal shear stress, yield zone shaded. Lower diagram plots maximum principal normal stress, tension zone shaded. Contact radius AA.

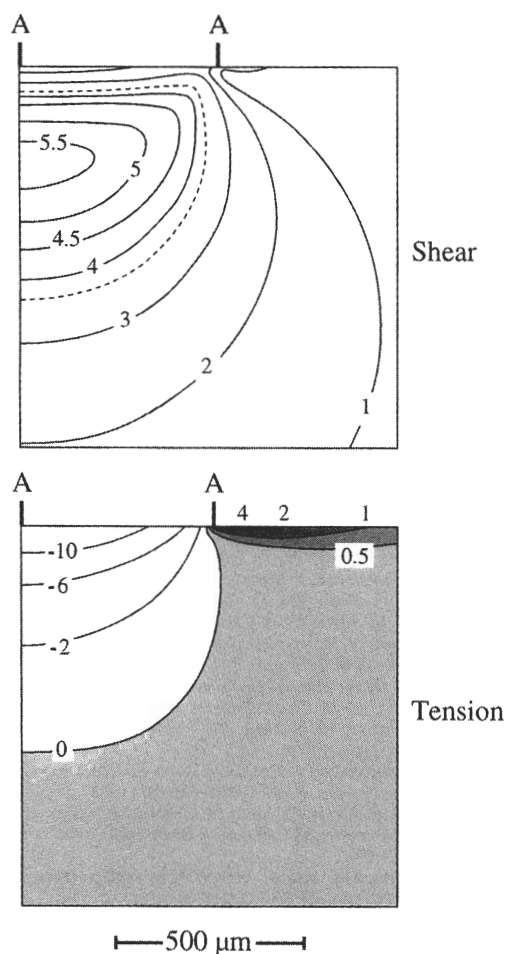


Fig. 13. Same as Fig. 12, but computed for hypothetical elastic silicon nitride ($\alpha = 1$). Note sustained buildup of shear stress within previous yield zone (dashed), inward expansion of subsurface tensile stress zone outside contact. Contact radius AA.

interpreted as the critical resolved shear stress at first slip ("cohesion stress"); strain-hardening coefficient α measures the local elastic constraint, strain-invariant in the approximation of noninteracting faults (linear hardening).¹⁷ Such models open up the prospect of incorporating key microstructural variables (e.g., volume fraction of second phase, grain size and shape, interboundary toughness, internal residual stresses) into the macroscopic stress-strain characteristic, specifically through the α term,¹⁷ and thence of tailoring materials to optimize contact damage resistance.

The present study provides a basis for extending plasticity theory to tough ceramics. Central to this extension is allowance for a greater role of elastic constraint in the formation geometry.^{20,25,28} An increased yield stress to modulus Y/E manifests itself as a greater constriction on the quasi-plastic zone, i.e., an enhanced *macroscopic* constraint. This increased constraint is evident in the progression steel-glass-ceramic-silicon nitride in Figs. 9 to 11. Likewise, an increased strain-hardening coefficient α reflects a greater constriction on slip from discrete shear faults,¹⁷ i.e., an enhanced *microscopic* constraint. Compare the sustained buildup of stress within the yield zone in the purely elastic silicon nitride in Fig. 13 with that in the quasi-plastic silicon nitride in Fig. 12. The complex deformation zone configurations that characterize ceramics thereby preclude the use of the simpler contact plasticity models, such as the radially symmetric expanding cavity model.^{20,25,26,28} They also preclude retention of the powerful concept of geometrical similarity widely used to estimate yield stresses from hardness measurements, so that the constraint factor $c = H/Y$, with value ≈ 3 in

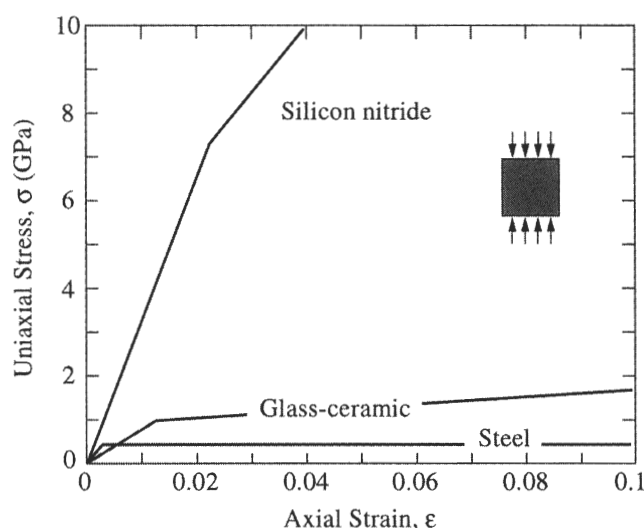


Fig. 14. Deconvoluted intrinsic stress-strain curves for soft steel, micaceous glass-ceramic, and heterogeneous silicon nitride, for uniform uniaxial loading state (inset).

ideally elastic solids,²⁰ can no longer be expected to remain material-invariant in ceramics.²⁷

As a tool for analyzing contact stress fields, the FEM algorithm used here suffers from the same limitations as all other numerical procedures. At the same time, FEM is entirely objective in the way it deals with complex deformation zone geometries in ceramics. Moreover, it enables extraction of fundamental material stress-strain information, and provides certain insights into the factors responsible for the transition from brittleness to quasi-plasticity,¹ as follows:

(i) By best-fitting the experimental $p_0(a/r)$ data (Figs. 1 to 4), the intrinsic constitutive stress-strain curves that would obtain in uniaxial compression in the absence of brittle fracture can be deconvoluted, in our case within the confines of linear strain-hardening and the bounds of combined experimental and computational uncertainty ($\approx 10\%$ in strain and $\approx 20\%$ in stress, Sections IIB and IIIA). We plot such deconvoluted curves in Fig. 14 for the test materials used in the present study, using the calibrated parameters in Table I.

(ii) The computed yield zone boundaries in Figs. 9 to 11 reproduce all the essential macroscopic features of the damage evolution in the micrographs of Fig. 5 to 7. The more detailed contour map for silicon nitride in Fig. 12 reveals how the introduction of heterogeneity (cf. hypothetical elastic silicon nitride in Fig. 13) relaxes shear stresses within the quasi-plastic zone (Section III(3)).

Notwithstanding the degree of agreement achieved between experimental and computed contact zones in the present study, it is important to emphasize that issues remain concerning the fundamental nature and geometry of quasi-plastic deformation in tough ceramics. For instance, it is implicit in our adoption of Eq. (1) within the FEM code that the deformation is exclusively shear driven. In some polycrystalline ceramics like alumina, extreme stress concentrations at the ends of intragrain twin shear faults can initiate microcracks along weak grain boundaries.^{7,50} Such microcracks can extend during the release of elastic compression stresses during unloading, and ultimately coalesce, resulting in greater compliance and a consequent downturn in the intrinsic uniaxial stress-strain curve.² The indications from the curves in Figs. 2 and 4 are that no such softening region is attained in the present ceramics, at least over the load ranges covered in the present study. Other, more extraneous factors in the contact boundary conditions, such as interfacial friction, could have an additional modifying effect on the deformation geometry in cases of extreme sphere/specimen elastic mismatch.⁵¹

Studies of quasi-plasticity beneath Hertzian contacts in ceramics offer the prospect of a predictive basis for engineering and materials design. The engineering relevance of such studies to bearing problems, and to associated impact damage, fatigue, and wear properties, is immediate. The FEM methodology is not limited by configurational complexities in the contact deformation pattern, so consideration of even more complex contact loading geometries (e.g., sliding and rolling contacts) and specimen geometries (duplex structures, such as laminates) would appear to be a logical extension. From the materials standpoint, the capacity to extract intrinsic stress-strain data, in combination with independent micromechanical modeling,¹⁷ foreshadows the tailoring of ordinarily brittle ceramic microstructures, via controlled heterogeneity, for specific damage tolerance applications.

Acknowledgments: We wish to acknowledge the following original sources of some of the data used in this study: H. Cai, F. Guiberteau, N. P. Padture, A. Pajares, M. A. Stevens Kalceff, and H. H. K. Xu.

References

- ¹B. R. Lawn, N. P. Padture, H. Cai, and F. Guiberteau, "Making Ceramics 'Ductile'," *Science*, **263**, 1114–16 (1994).
- ²J. C. Jaeger and N. G. W. Cook, *Fundamentals of Rock Mechanics*. Chapman and Hall, London, U.K., 1971.
- ³M. S. Paterson, *Experimental Rock Deformation—The Brittle Field*. Springer-Verlag, Berlin, Germany, 1978.
- ⁴H. Horii and S. Nemat-Nasser, "Brittle Failure in Compression: Splitting, Faulting and Brittle-Ductile Transition," *Philos. Trans. R. Soc. London*, **319** [1549] 337–74 (1986).
- ⁵M. F. Ashby and S. D. Hallam, "The Failure of Brittle Solids Containing Small Cracks Under Compressive Stress States," *Acta Metall. Mater.*, **34** [3] 497–510 (1986).
- ⁶F. Guiberteau, N. P. Padture, H. Cai, and B. R. Lawn, "Indentation Fatigue: A Simple Cyclic Hertzian Test for Measuring Damage Accumulation in Polycrystalline Ceramics," *Philos. Mag. A*, **68** [5] 1003–16 (1993).
- ⁷F. Guiberteau, N. P. Padture, and B. R. Lawn, "Effect of Grain Size on Hertzian Contact in Alumina," *J. Am. Ceram. Soc.*, **77** [7] 1825–31 (1994).
- ⁸H. Cai, M. A. Stevens Kalceff, and B. R. Lawn, "Deformation and Fracture of Mica-Containing Glass-Ceramics in Hertzian Contacts," *J. Mater. Res.*, **9** [3] 762–70 (1994).
- ⁹H. Cai, M. A. S. Kalceff, B. M. Hooks, B. R. Lawn, and K. Chyung, "Cyclic Fatigue of a Mica-Containing Glass-Ceramic at Hertzian Contacts," *J. Mater. Res.*, **9** [10] 2654–61 (1994).
- ¹⁰N. P. Padture and B. R. Lawn, "Toughness Properties of a Silicon Carbide with an *In-Situ*-Induced Heterogeneous Grain Structure," *J. Am. Ceram. Soc.*, **77** [10] 2518–22 (1994).
- ¹¹N. P. Padture and B. R. Lawn, "Contact Fatigue of a Silicon Carbide with a Heterogeneous Grain Structure," *J. Am. Ceram. Soc.*, **78** [6] 1431–38 (1995).
- ¹²N. P. Padture and B. R. Lawn, "Fatigue in Ceramics with Interconnecting Weak Interfaces: a Study Using Cyclic Hertzian Contacts," *Acta Metall.*, **43** [4] 1609–17 (1995).
- ¹³H. H. K. Xu, L. Wei, N. P. Padture, B. R. Lawn, and R. L. Yeckley, "Effect of Microstructural Coarsening on Hertzian Contact Damage in Silicon Nitride," *J. Mater. Sci.*, **30**, 869–78 (1995).
- ¹⁴P. L. Swanson, C. J. Fairbanks, B. R. Lawn, Y.-W. Mai, and B. J. Hockey, "Crack-Interface Grain Bridging as a Fracture Resistance Mechanism in Ceramics: I, Experimental Study on Alumina," *J. Am. Ceram. Soc.*, **70** [4] 279–89 (1987).
- ¹⁵S. J. Bannison and B. R. Lawn, "Role of Interfacial Grain-Bridging Sliding Friction in the Crack-Resistance and Strength Properties of Nontransforming Ceramics," *Acta Metall.*, **37** [10] 2659–71 (1989).
- ¹⁶S. J. Bannison, N. P. Padture, J. L. Runyan, and B. R. Lawn, "Flaw-Insensitive Ceramics," *Philos. Mag. Lett.*, **64** [4] 191–95 (1991).
- ¹⁷A. C. Fischer-Cripps and B. R. Lawn, "Indentation Stress-Strain Curves for 'Quasi-Ductile' Ceramics," *Acta Metall.*, **44** [2] 519–27 (1996).
- ¹⁸A. Pajares, F. Guiberteau, B. R. Lawn, and S. Lathabai, "Hertzian Contact Damage in Magnesia-Partially-Stabilized Zirconia," *J. Am. Ceram. Soc.*, **78** [4] 1083–86 (1995).
- ¹⁹B. R. Lawn and T. R. Wilshaw, "Indentation Fracture: Principles and Applications," *J. Mater. Sci.*, **10** [6] 1049–81 (1975).
- ²⁰D. Tabor, *Hardness of Metals*. Clarendon, Oxford, U.K., 1951.
- ²¹A. Pajares, L. Wei, B. R. Lawn, and D. B. Marshall, "Damage Accumulation and Cyclic Fatigue in Mg-PSZ at Hertzian Contacts," *J. Mater. Res.*, **10** [10] 2613–25 (1995).
- ²²N. P. Padture, C. J. Evans, H. H. K. Xu, and B. R. Lawn, "Enhanced Machinability of Silicon Carbide via Microstructural Design," *J. Am. Ceram. Soc.*, **78** [1] 215–17 (1995).
- ²³H. H. K. Xu and S. Jahanmir, "Scratching and Grinding of a Machinable Glass-Ceramic with Weak Interfaces and Rising *T*-Curve," *J. Am. Ceram. Soc.*, **78** [2] 497–500 (1995).
- ²⁴H. H. K. Xu, N. P. Padture, and S. Jahanmir, "Effect of Microstructure on Scratching and Grinding Responses of Silicon Carbide Ceramics," *J. Am. Ceram. Soc.*, **78** [9] 2443–48 (1995).
- ²⁵K. L. Johnson, *Contact Mechanics*. Cambridge University Press, London, U.K., 1985.
- ²⁶R. Hill, *The Mathematical Theory of Plasticity*. Oxford University Press, London, U.K., 1950.
- ²⁷M. V. Swain and J. T. Hagan, "Indentation Plasticity and the Ensuing Fracture of Glass," *J. Phys. D*, **9**, 2201–14 (1976).
- ²⁸D. M. Marsh, "Plastic Flow and Fracture in Glass," *Proc. R. Soc. London*, **A282** [1388] 33–43 (1964).
- ²⁹S. S. Chiang, D. B. Marshall, and A. G. Evans, "The Response of Solids to Elastic/Plastic Indentation. I. Stresses and Residual Stresses," *J. Appl. Phys.*, **53** [1] 298–311 (1982).
- ³⁰K. Komvopoulos, "Elastic-Plastic Finite Element Analysis of Indented Layered Media," *J. Tribol.*, **111**, 430–39 (1989).
- ³¹P. Montmitonnet, M. L. Edinger, and E. Felder, "Finite Element Analysis of Elastoplastic Indentation: Part II—Application to Hard Coatings," *J. Tribol.*, **115**, 15–19 (1993).
- ³²A. C. Fischer-Cripps, "Elastic-Plastic Behaviour in Materials Loaded with a Spherical Indenter," *J. Mater. Sci.*, in press.
- ³³C. K. Chyung, G. H. Beall, and D. G. Grossman, "Microstructures and Mechanical Properties of Mica Glass-Ceramics"; pp. 1167–94 in *Electron Microscopy and Structure of Materials*. Edited by G. Thomas, R. M. Fulrath, and R. M. Fisher. University of California Press, Berkeley, CA, 1972.
- ³⁴K. Chyung, G. H. Beall, and D. G. Grossman, "Fluorophlogopite Mica Glass-Ceramics"; pp. 33–40 in *Proceedings of the 10th International Glass Congress*, No. 14. Edited by M. Kunugi, M. Tashiro, and N. Saga. Ceramic Society of Japan, Kyoto, Japan, 1974.
- ³⁵R. M. Davies, "Determination of Static and Dynamic Yield Stresses Using a Steel Ball," *Proc. R. Soc. London*, **A197** [1050] 416–32 (1949).
- ³⁶M. V. Swain and B. R. Lawn, "A Study of Dislocation Arrays at Spherical Indentations in LiF as a Function of Indentation Stress and Strain," *Phys. Status Solidi*, **35** [2] 909–23 (1969).
- ³⁷T. O. Mulhearn, "The Deformation of Metals by Vickers-Type Pyramidal Indenters," *J. Mech. Phys. Solids*, **7**, 85–96 (1959).
- ³⁸H. Hertz, *Hertz's Miscellaneous Papers*; Chs. 5 and 6. Macmillan, London, U.K., 1896.
- ³⁹F. C. Frank and B. R. Lawn, "On the Theory of Hertzian Fracture," *Proc. R. Soc. London*, **A299** [1458] 291–306 (1967).
- ⁴⁰I.-W. Chen, "Implications of Transformation Plasticity in ZrO₂-Containing Ceramics: II, Elastic-Plastic Indentation," *J. Am. Ceram. Soc.*, **69** [3] 189–94 (1986).
- ⁴¹D. B. Marshall and M. V. Swain, "Crack-Resistance Curves in Magnesia-Partially-Stabilized Zirconia," *J. Am. Ceram. Soc.*, **71** [6] 399–407 (1988).
- ⁴²N. P. Padture, J. L. Runyan, S. J. Bannison, L. M. Braun, and B. R. Lawn, "Model for Toughness-Curves in Two-Phase Ceramics: II, Microstructural Variables," *J. Am. Ceram. Soc.*, **76** [9] 2241–47 (1993).
- ⁴³H. Cai, N. P. Padture, B. M. Hooks, and B. R. Lawn, "Flaw Tolerance and Toughness-Curves in Two-Phase Particulate Composites: SiC/Glass System," *J. Eur. Ceram. Soc.*, **13**, 149–57 (1994).
- ⁴⁴L. Wei and B. R. Lawn, "Thermal Wave Analysis of Contact Damage in Ceramics: Case Study on Alumina," *J. Mater. Res.*, **11** [4] 939–47 (1996).
- ⁴⁵M. L. Batzle, G. Simmons, and R. W. Siegfried, "Microcrack Closure in Rocks Under Stress: Direct Observations," *J. Geophys. Res.*, **85** [B12] 7072–90 (1980).
- ⁴⁶R. L. Kranz, "Microcracks in Rocks: A Review," *Tectonophysics*, **100**, 449–80 (1983).
- ⁴⁷J. M. Kemeny and N. G. W. Cook, "Micromechanics of Deformation in Rock"; pp. 287–311 in *Toughening Mechanisms in Quasi-Brittle Materials*. Edited by S. P. Shah. Kluwer Academic Publishers, Dordrecht, Netherlands, 1991.
- ⁴⁸L. R. Myer, J. M. Kemeny, Z. Zheng, R. Suarez, R. T. Ewy, and N. G. W. Cook, "Extensive Cracking in Porous Rock under Differential Compressive Stress," *Appl. Mech. Rev.*, **45** [8] 263–80 (1992).
- ⁴⁹T.-F. Wong, H. Szeto, and J. Zhang, "Effect of Loading Path and Porosity on the Failure Mode of Porous Rocks," *Appl. Mech. Rev.*, **45** [8] 281–93 (1992).
- ⁵⁰B. R. Lawn, N. P. Padture, F. Guiberteau, and H. Cai, "A Model for Microcrack Initiation and Propagation Beneath Hertzian Contacts in Polycrystalline Ceramics," *Acta Metall.*, **42** [5] 1683–93 (1994).
- ⁵¹K. L. Johnson, J. J. O'Connor, and A. C. Woodward, "The Effect of Indenter Elasticity on the Hertzian Fracture of Brittle Materials," *Proc. R. Soc. London*, **A334**, 95 (1973). □